Photochemistry and Photobiology, 2011, 87: 408–417

Multiphoton Imaging of Actin Filament Formation and Mitochondrial Energetics of Human ACBT Gliomas

Yu-Jer Hwang[1,2], Nomiki Kolettis[1,2], Miso Yang[2], Elizabeth R. Gillard[2], Edgar Sanchez[3], Chung-Ho Sun[4], Bruce J. Tromberg[4], Tatiana B. Krasieva[4] and Julia G. Lyubovitsky[*2]

[1]Cell Molecular and Developmental Biology Program, University of California, Riverside, Riverside, CA
[2]Bioengineering Department, University of California, Riverside, Riverside, CA
[3]Department of Biological Engineering, MIT, Cambridge, MA
[4]Beckman Laser Institute, Irvine, CA

Received 27 August 2009, accepted 10 November 2010, DOI: 10.1111/j.1751-1097.2010.00873.x

ABSTRACT

We studied the three-dimensional (3D) distribution of actin filaments and mitochondria in relation to ACBT glioblastoma cells migration. We embedded the cells in the spheroid form within collagen hydrogels and imaged them by *in situ* multiphoton microscopy (MPM). The static 3D overlay of the distribution of actin filaments and mitochondria provided a greater understanding of cell-to-cell and cell-to-substrate interactions and morphology. While imaging mitochondria to obtain ratiometric redox index based on cellular fluorescence from reduced nicotinamide adenine dinucleotide and oxidized flavin adenine dinucleotide we observed differential sensitivity of the migrating ACBT glioblastoma cells to femtosecond laser irradiation employed in MPM. We imaged actin-green fluorescent protein fluorescence in live ACBT glioma cells and for the first time observed dynamic modulation of the pools of actin during migration in 3D. The MPM imaging, which probes cells directly within the 3D cancer models, could potentially aid in working out a link between the functional performance of mitochondria, actin distribution and cancer invasiveness.

INTRODUCTION

Biomedical imaging using multiphoton microscopy (MPM) combines backscattered second harmonic generation (SHG) and two-photon fluorescence (TPF) signals. Combined TPF and SHG have been widely employed to nondestructively obtain structural and functional information at depth in thick, living tissues with high resolution and contrast (1–23).

This report establishes the development of MPM methods in following the behavior of glioma tumors in their three-dimensional (3D) surroundings aimed to emulate the *in vivo* environments. This information will allow characterizing various features of glioma tumors including cell–cell and extracellular matrix (ECM)–cell interactions as well as the functional performance of mitochondria while linking that performance with cancer invasiveness. Ultimately it will help to noninvasively evaluate and/or to enhance the efficacy of glioma tumors treatment.

Gliomas are a heterogenous group of the central nervous system (CNS) tumors that can be classified as one of several types: astrocytomas, oligodendrogliomas, medulloblastomas and ependymomas. Gliomas account for 51% of CNS tumors; of these, the astrocytomas are the most common (24,25). These neoplasms are believed to arise from astrocytes, a type of glial cell that plays a variety of important supportive roles in neuronal function, or from astrocyte precursor cells and/or cancer stem cells (26,27). Astrocytomas are further subclassified as low-grade astrocytomas, anaplastic astrocytomas and glioblastomas. Among the astrocytomas, glioblastoma multiforme is the most commonly diagnosed (24,25), the most aggressive and fatal tumor (28). Patients diagnosed with such gliomas often have a life expectancy of less than 1 year. In many patients, the removal of this type of tumor is not feasible because the tumor is located in a critical brain area. In the 10–15% of patients who can undergo surgery, recurrence is likely in 80% of the cases (29). Chemotherapy and radiation therapy have poor efficacy and fail mostly because residual tumor cells become resistant to treatments.

The poor prognosis of glioblastoma patients results directly from the unusual behavior of glioma cells. Glioma cells display an extraordinary invasiveness into the healthy brain tissue, which suggests that they are integrating very efficiently energy balance, cytoskeletal rearrangements and secretory activity during migration. To migrate, tumor cells generally undergo cytoskeletal remodeling to elongate in the direction of migration with pseudopodia, lamellipodia, filopodia and invadopodia forming at the leading invasive edges (30), form transient attachments to the ECM, modify ECM by tumor-secreted proteins, such as tenascin-C and degrade ECM by secreted proteases (30). Actin polymerization at the leading edges appears to be critical for the cytoskeletal extensions and ECM attachments as well as movement and localization of mitochondria in the areas of energy-intense locations (31).

We herein report several interesting behaviors of ACBT glioma cells migrating within the 3D hydrogels aimed to emulate the *in vivo* environments. We characterized the cells' behaviors by *in situ* MPM. Our models utilize solid spheroids (*i.e.* compact cluster of live cells and dead cells of a necrotic core) embedded

*Corresponding author e-mail: julial@ucr.edu (Julia G. Lyubovitsky)
© 2011 The Authors
Photochemistry and Photobiology © 2011 The American Society of Photobiology 0031-8655/11

in 3D ECMs. These models have been employed to mimic microtumors and metastases (32). Similar to malignant gliomas *in vivo* (33–35), these *in vitro* models contain a large central core of extensive necrosis surrounded by a dense shell of invasive cells that migrate into surrounding ECMs (36).

We find that the sensitivity of ACBT glioblastoma cells migrating in 3D to femto-second laser irradiation is not uniform. *In situ* multiphoton ratiometric redox imaging based on cellular fluorescence from reduced nicotinamide adenine dinucleotide (NADH) and oxidized flavin adenine dinucleotide (FAD) detects at least two different populations of migrating ACBT glioblastoma cells. One population of cells maintains original morphology after the 3D imaging, as well as retains functional mitochondria. Disrupted cellular membranes characterize another population. An *in situ* F-actin and mitochondrial stains' fluorescence provides a new insight into the cell-to-cell and cell-to-substrate interactions and morphology in 3D. The actin-green fluorescent protein (GFP) fluorescence dynamically spreads through the cell body into the lamellipodia when we follow the pattern of the real time reorganization of actin. Temporary pools or ''globes'' of actin are observed for the first time and are thought to represent G-actin generated to facilitate cellular movement along the collagen fibers of the ECM.

MATERIALS AND METHODS

Three-dimensional glioblastoma model. The human grade IV glioblastoma cell line (ACBT) was a generous gift of G. Granger (University of California at Irvine, CA). The cells were cultured as in Ref. (37). Spheroids were grown according to standard procedures (38). To prepare our 3D models, ACBT glioma spheroids were visually selected according to size. Unless noted, each spheroid selected for the studies presented in this report was 500 μm in diameter.

To ensure that the ACBT glioma spheroids properly attached to the Petri dishes, 3 μL of rat tail type I collagen gel (BD Biosciences, 2 mg mL^{-1}) was placed in the middle of the dish. Using a sterile white rubber policeman, the collagen was then evenly distributed. While the collagen was left to dry for an hour, ACBT glioma spheroids were selected. Once the collagen dried, one ACBT glioma spheroid was placed in each Petri dish along with 2 mL of the growth medium Dulbecco's Modified Eagle Medium (DMEM; Gibco Cat. No. 12800-058, 1×). One hour of incubation (37°C, 5% CO_2) followed to ensure that the spheroid properly attached to the layer of collagen. Using this procedure we could ensure that we were using only the spheroids that were able to attach to the collagen layer.

An ice-cold collagen mix was then prepared consisting of 700 μL of 4.52 mg mL^{-1} collagen type I, 100 μL of reconstitution buffer (10×) and 200 μL of DMEM growth medium (Gibco Cat. No. 12800-058, 5×). The 10× reconstitution buffer was prepared by combining 2.2 g of $NaHCO_3$ (tissue culture grade) and 4.77 g HEPES (tissue culture grade, Gibco Cat. No 845-1344) in a 100 mL medium bottle, adding 75 mL of 0.05 *N* NaOH (5 mL of 1 *N* NaOH [Fisher, SS266-1] added to a 95 mL doubly distilled, deionized water) to the sodium bicarbonate and HEPES powder, mixing well to dissolve and bringing the solution to the final volume of 100 mL with 0.05 *N* NaOH. The buffer was filter sterilized with 0.22 μm filter into a sterile medium bottle and stored at 4°C.

After visually confirming spheroid attachment, the initial DMEM medium (1×) was carefully replaced with 200 μL of the ice-cold collagen mix and incubated (37°C, 5% CO_2) for 30 min. Two milliliters of DMEM growth medium with all the essential supplements (1×) was then added to each sample to cover the spheroid. The samples were placed back in the incubator.

Mitochondrial stain: MitoTracker Orange CM-H_2TMRos. To prepare 1 mM stock solution, 50 μg of lyophilized CM-H_2TMRos (Molecular Probes, M-7511) was dissolved in 130 μL of high-quality, anhydrous dimethyl sulfoxide. The stock solution was diluted with DMEM growth medium to the final 1300 nM working solution. The dye uptake was followed by monitoring 580 nm fluorescence of the fluorescent CM-H_2TMRos cationic form. After 1 h of incubation, the fluorescence level was low. As judged by morphology, staining for up to 22 h could be performed with no toxicity to the ACBT glioma spheroids. Photobleaching of fluorescent oxidized dye was low upon prolonged (20 min) two-photon excitation.

F-actin stain: Alexa Flour 488 Phalloidin. The F-actin stain selected was the Alexa Flour 488 Phalloidin (A12379, Invitrogen). The phallotoxin is isolated from the deadly *Amanita phalloides* mushroom as a bicyclic peptide that competitively binds to F-actin sites (39). The labeled phallotoxins have the same affinity for both large and small filaments, and inside cells, one phallotoxin molecule binds per actin subunit. The one-photon excitation maximum of the Alexa Flour 488 Phalloidin is at 495 nm and its emission is at 518 nm (39).

After the mitochondrial stain, the cell model was fixed with formaldehyde. The medium was replaced with 3 mL of 4% formaldehyde and samples were left at 4°C overnight. After fixation, the 3D ACBT models were washed three times with PBS (pH 7.4), with 15 min equilibration periods between each rinse, and then permeabilized with 0.1% Triton X-100 (in PBS, pH 7.4) for 1 h prior to F-Actin staining. Samples were then rinsed five times with PBS with 15 min equilibration periods.

A stock solution of F-actin stain (Invitrogen) was prepared by taking 1 vial of 300 units of lyophilized solid compound and dissolving it in 1.5 mL of methanol to yield a final concentration of 200 units mL^{-1} (6.6 μM); 50 μL of F-actin stock solution was diluted into 2 mL of PBS and added to each sample. The 3D ACBT models were then incubated at 4°C for 16–20 h. Upon completion, samples were washed for a total of five times with PBS with 1 h equilibration periods between each wash. Imaging of 3D ACBT glioma models was performed as described in the subsection entitled *MPM: Ratiometric imaging and spectra* in this section.

F-actin live stain: Transduction with actin-GFP reagent. ACBT cells were plated and were grown overnight as a monolayer. Transduction solution was prepared by combining 2 parts of CellularLights actin-GFP reagent (component A, Invitrogen C10126) with 3.5 parts of Dulbecco's PBS (D-PBS) without calcium and magnesium. After the next day's replacement of the growth medium with transduction solution, the cells were kept at room temperature in the dark for 3 h with gentle shaking. The transduction solution was then replaced with enhancer solution prepared by combining growth medium with 1× BacMam enhancer (component B) and kept for another 2 h in the culture incubator at 37°C and 7.5% CO_2. The enhancer solution was replaced with growth medium and cells were subsequently incubated for 24 h to allow the expression of actin-GFP. Transduced cells were harvested and plated in Petri dish at high density (about 1 million cells per 60 mm dish) at least overnight to allow spheroid formation. The 3D glioma models were then formed as described in the subsection entitled *Three-dimensional glioblastoma model* in this section.

MPM: Ratiometric imaging and spectra. The inverted muliphoton laser scanning microscope used in this work is described elsewhere (9,40–42). Briefly, the system consisted of a Kerr-lens mode-locked Ti:sapphire oscillator (Mira 900F; 200 fs pulse width, 76 MHz repetition rate; Coherent) pumped by a frequency-doubled 5 W Nd:YVO_4 solid-state laser (Verdi, Coherent). Spectra were acquired with a SpectraPro-150 spectrograph equipped with a 300 grooves mm^{-1} grating blazed at 500 nm (Acton Research Corp.), and a high dynamic range MicroMax: 512BFT CCD camera (Princeton Instruments) controlled by an ST-133 Controller (Princeton Instruments). The spectrograph and camera settings were PC-controlled through commercially available software (WinSpec/32 v. 2.4.6.6, Roper Scientific, Inc.). The CCD temperature was maintained at −45°C. The entrance slit of the spectrograph was set to a width of 0.5 mm.

In all the experiments, the laser excitation was linearly polarized at the selected excitation wavelength and verified with a β-barium borate nonlinear crystal placed on the microscope stage. Experimental error in the fluorescence and SHG measurements because of instrument setting parameters was established using fluorescein solutions and SHG nonlinear crystals (*z*-cut quartz and others), respectively. Experimental variability between measurements because of instrument setting parameters was found to be less than about 3%. The samples were imaged using Zeiss objectives under standard thickness coverglass. We used 10× air (NA = 0.33) and 40× water (NA = 0.8) for quantitative work and 63× water (NA = 1.2), as well as 100× water

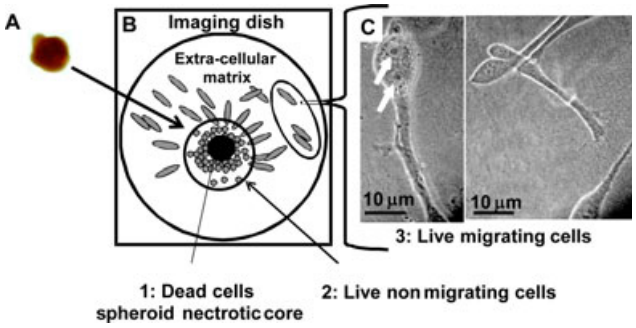

Figure 1. The three-dimensional (3D) ACBT glioblastoma model. (A) *En face* micrograph of ACBT glioblastoma spheroid used in the development of 3D ACBT glioblastoma model. (B) Generalized and schematic overview of the model. (C) Confocal reflectance mode bright-field microscopy images of the ACBT glioma cells migrating within the 3D collagen hydrogels. The cells are mostly double-nucleated (arrows point to the nuclei).

(NA = 1.0) for high-resolution imaging. Spectral filtering with a 500 nm dichroic beamsplitter and a bandpass filter (400AF10 for λ_{ex} = 800 nm) were used to separate the SHG of the ECM from that of intrinsic fluorescence. The autofluorescence was further separated into blue (using 445 ± 25 nm filter for λ_{ex} = 770 nm) and red (using 580 ± 30 nm filter for λ_{ex} = 770 nm) components to be detected by the corresponding PMTs. Binary data was converted to 16-bit TIFF images using IPLab software (Scanalytics, Inc.). Three-dimensional reconstructions of 3D ACBT glioblastoma models and all corresponding sections were obtained using IPLAB (Scanalytics, Inc.) and VoxBlast software (VayTek, Inc.). Multiphoton ratiometric values were calculated using Matlab. The intensity values of all $256 \times 256 = 65\,536$ pixels were added for blue and red channels separately. Subsequently, ratios were obtained by dividing the total intensity of all pixel values for the blue channel by that for the red channel. The background noise in photon counting data collection mode used was low; therefore, this approach for obtaining multiphoton ratiometric values was acceptable. Additionally, while the fluorescence of NADH and FAD themselves may be affected by instrument setting parameters, laser instability and possible sampling artifacts, their ratio effectively eliminates the measurement errors and therefore can provide useful, reliable information regarding the redox properties of the cells.

Multiphoton autofluorescence from different cells and samples prepared on separate days was evaluated. The conditions of samples and cellular morphology were matched as closely as possible. Only cells that migrated away from the solid spheroid and had lamellipodia and shapes similar to the cells in Fig. 1C were evaluated. Prior to measurements, the phenol-containing media were removed and 3D glioblastoma models were washed three times with PBS. In Alexa Flour 488 Phalloidin imaging experiments, 800 nm excitation wavelength was employed and the emission was detected through the 500–550 bandpass filter. In MitoTracker Orange CM-H_2TMRos mitochondrial imaging experiments 800 nm excitation wavelength was used, and the emission was observed with a 550–610 nm bandpass filter.

LSM 510 confocal microscopy: Live actin-GFP imaging. The Zeiss LSM 510 NLO meta microscopy system is based on an Axiovert 200 M inverted microscope equipped with standard illumination systems for transmitted light and epi-fluorescence detection and a standard set of visible light lasers, including an Argon laser 458/477/488/514 nm/30 mW for confocal microscopy. It is equipped with an NLO interface for a femtosecond Ti:sapphire laser excitation source (Chameleon-Ultra, Coherent) for multiphoton excitation with the exceptional tunability range from 690 to 1040 nm. The instrument is equipped with two single-channel PMT detectors, the META polychromatic detector and a transmission light channel. The microscope platform is equipped with a motorized *X–Y* scanning stage and long-working distance and high numerical aperture objectives (20, 40 and 100×). Software supports time-lapse sequence automatic acquisition.

RESULTS

Three-dimensional ACBT glioblastoma model

Our models utilize solid spheroids (*i.e.* compact cluster of live cells and dead cells of a necrotic core) embedded in 3D ECMs (Figs. 1A,B). A typical spheroid of 500 μm in diameter (Fig. 1A) is surrounded by ECM in the generalized and schematic overview of the model shown in Fig. 1B. This work focused on live migrating cells (Fig. 1C) that exhibited lamellipodia while migrating within ECMs. They were mostly double-nucleated (Fig. 1C, arrows point to the nuclei), migrated in clusters and visibly interacted with other nearby cells and ECM.

Multiphoton imaging of mitochondria

We first explored the utility of a multiphoton ratiometric redox fluorometry approach based on cellular fluorescence from reduced NADH and oxidized FAD to study mitochondrial energy metabolism (42) within live migrating populations of ACBT glioblastoma cells. The visualized mitochondria appeared in the form of clusters mostly 1–2 μm in diameter and punctuate structures (Fig. 2A, white arrows). For the majority of mitochondrial clusters, the fluorescence was equally distributed between blue (445 ± 25 nm filter) and red (580 ± 30 nm) channels. Generally, only a few mitochondrial clusters inside a single glioma cell would fluoresce mostly in the blue channel.

Because mitochondria are three-dimensional organelles, we obtained their 3D reconstructed images by collecting *z*-stacks of the entire cells. The cells were about 10–15 μm thick. For most ACBT glioblastoma cells migrating within 3D matrices, the long cellular protrusions were highly convoluted in three dimensions. This complex cellular morphology manifested itself in low intensity of NADH and FAD signals from the lamellipodia (Fig. 2A, leftmost panel), which made the lamellipodia-associated fluorescence data less robust.

We used the images to evaluate NADH/FAD multiphoton ratiometric values and detected redox index profiles as a function of depth within individual cells. Figure 2B was constructed by averaging the ratios obtained from five most intensely fluorescing *x–y* optical sections inside the cells (*e.g.* alike to one in Fig. 2A, middle panel). The average mitochondrial redox index was 0.9 (Fig. 2B). Additionally, there was a subset of live migrating ACBT glioma cells that suffered nonreversible damage during prolonged acquisition of 3D tomographic data, which was aimed to achieve high signal-to-noise ratio. This subset constituted about 40% of all cells sampled and the metabolic redox index obtained for this subset was 0.6 (Fig. 2B).

To confirm that target structures within undisrupted cells were normally functioning mitochondria, we spectroscopically followed uptake of Rosamine MitoTracker Orange CM-H_2TMRos dye by ACBT glioma cells (Fig. 3). The initial form of the dye was nonfluorescent; however, it got oxidized into a fluorescent cationic form, and through a thiol conjugation became a fluorescent conjugate form. The uptake of the dye into the mitochondria took approximately 2 h as seen in Fig. 3A. The photobleaching rate of this dye once incorporated into active mitochondria was negligible. As previously

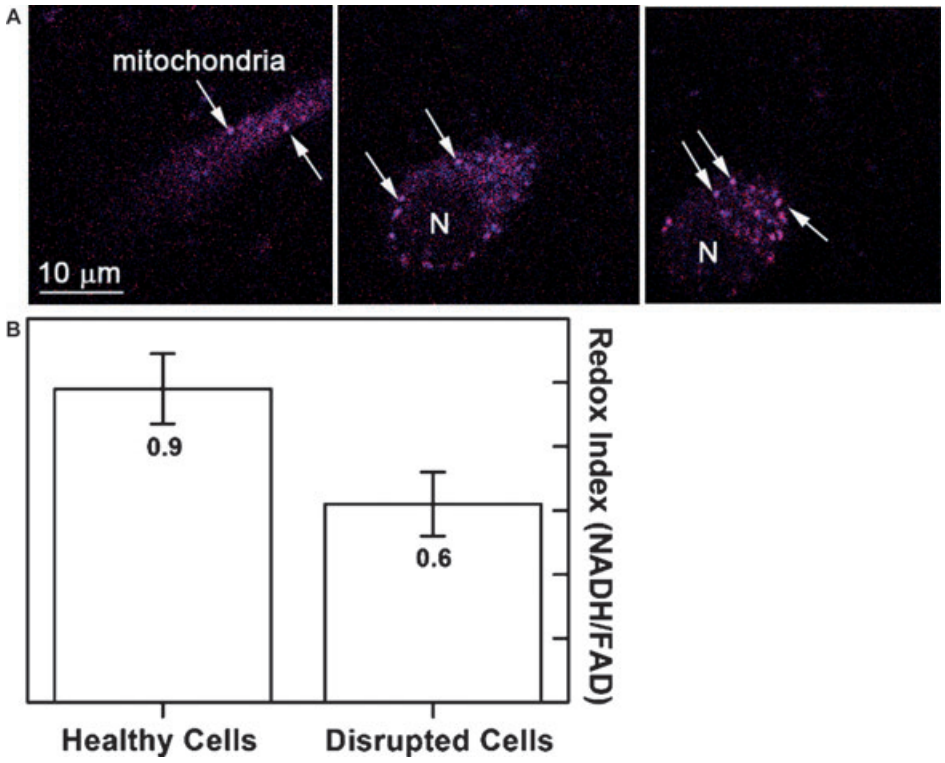

Figure 2. The multiphoton ratiometric redox fluorometry imaging of the ACBT glioma cells in the three-dimensional glioblastoma model. λ_{ex} = 770 nm. Focusing objective (Zeiss; 63× water immersion; NA is 1.2) was used to collect 35 μm × 35 μm images. (A) Multiphoton images of mitochondrial structures within ACBT glioma cells (left, bottom of a cell; right, top of a cell). White arrows indicate mitochondrial punctuate structures and clusters. Multiphoton excited ratio imaging: blue, NADH; pink, FAD. The two colors are superimposed. (B) Multiphoton redox ratiometric values for normal and disrupted cells.

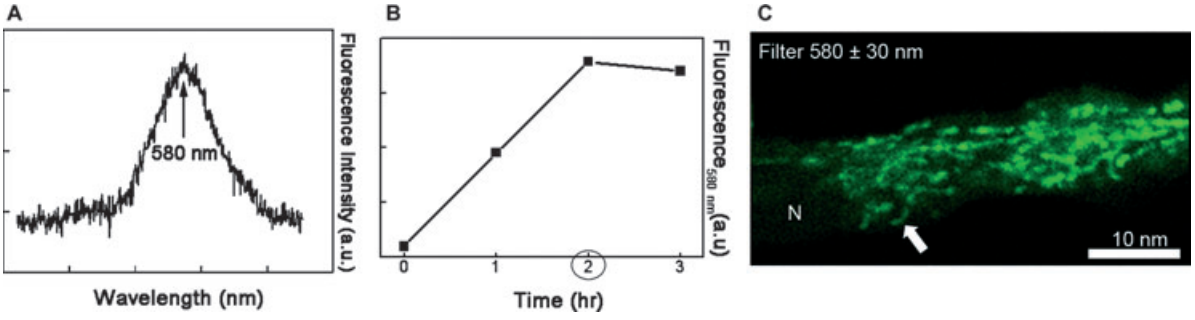

Figure 3. Rosamine MitoTracker Orange dye uptake by mitochondria and dye distribution within live ACBT glioma cells. (A) A typical fluorescence spectrum of the Rosamine MitoTracker Orange dye incorporated into the glioma cells with live mitochondria. (B) The time course for a typical uptake of the MitoTracker Orange dye into the glioma cells of three-dimensional model is shown to be complete in 2–3 h. (C) Multiphoton images of mitochondrial morphology within live migrating ACBT glioma cells. Fluorescence emission was isolated through the 580 ± 30 nm bandpass filter.

observed with MitoTracker dyes (43), mitochondrial morphology within live migrating cells stained with MitoTracker Orange appeared tubular (Fig. 3C).

Covisualization of F-actin filament distribution with respect to live mitochondria and ECM

To study the distribution of F-actin filaments with respect to the functioning mitochondria of ACBT glioma cells in the 3D glioma spheroid model, we established costaining and visualization protocols using multiphoton optical microscopy. The F-actin stain clearly labeled the cell boundary (Fig. 4A). The mitochondrial stain MitoTracker Orange appeared to localize intracellularly (Fig. 4B). The surrounding collagen matrix (visualized with SHG) is shown in Fig. 4C. These 3D overlays of the dyes and ECM provided better understanding of the cell-to-cell and cell-to-substrate interactions and morphology. After fixation, the mitochondrial dye had clearly diffused throughout the cytoplasm of the cells (Fig. 4B). This MitoTracker Orange diffusion was because of fixation and permeabilization employed in F-actin staining (Sanchez and Lyubovitsky, unpublished data).

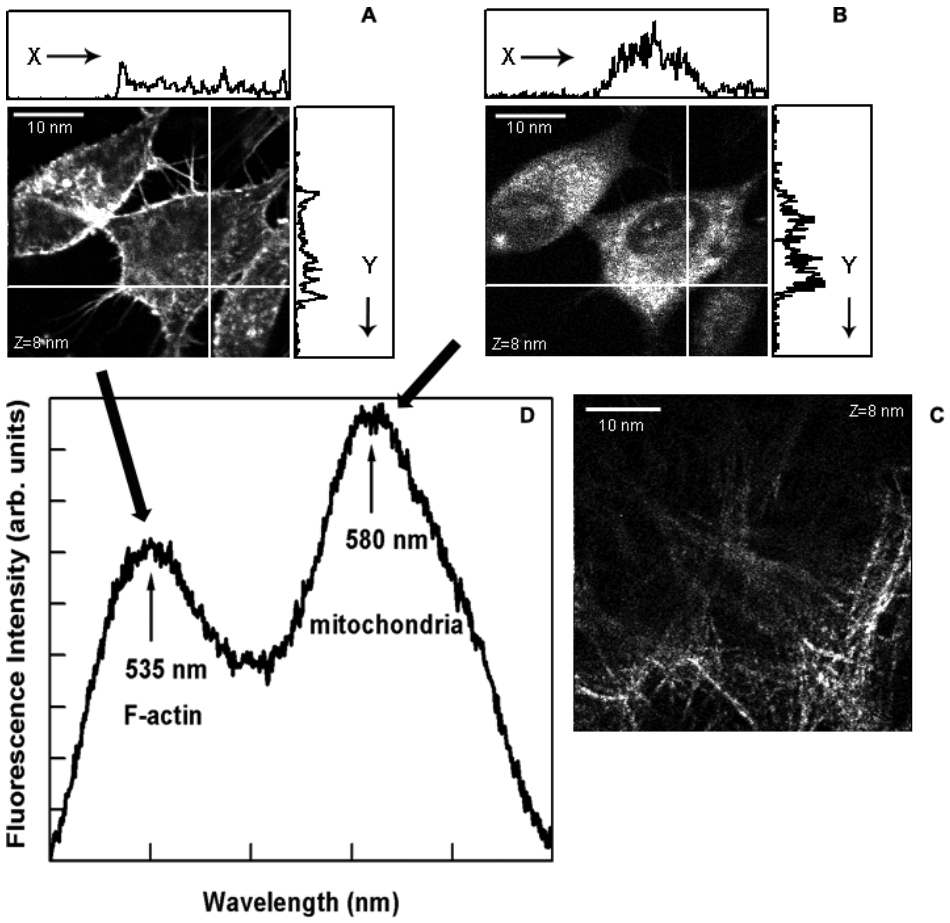

Figure 4. The distribution of F-actin filaments within cells with respect to live mitochondria and extracellular matrix in three-dimensional ACBT glioblastoma model. (A) Fluorescence generated by stained F-actin filaments located at exterior of the cells. Fluorescence emission was isolated through the 500–550 nm bandpass filter. (B) Fluorescence signal generated by MitoTracker Orange-stained mitochondria located in the cellular interior. Fluorescence emission was isolated through the 550–610 nm bandpass filter. (C) Second harmonic generation signal of surrounding collagen matrix. (D) Fluorescence spectrum showing the peaks for stained F-actin and stained mitochondria. All images and spectra were obtained from *en face* optical sections at 8 μm depth. Scale bars are 10 μm.

In many cases, F-actin filaments extended outward from the cells (Fig. 4A) and appeared anchored to the surrounding collagen (Fig. 4C). Additionally, cells participated in cell-to-cell interactions. For example, in Fig. 5, the *x–y* optical sections "cut" along the *z*-direction at 3 and 9 μm show the F-actin filaments anchoring one cell to another with multiple points of attachment. The sections collected at the depths of 3, 6, 7 and 9 μm display microspikes (filopodia; larger yellow arrows) extending from the cells.

The migrating cells as, for example, a cell shown in Fig. 6A, are characterized by rapid changes and production of stress fibers and lamellipodia. The sections of the cells that do not visibly change during migration contain microspikes and filopodia (ms/fil). Interestingly, during early stages of migration (3 days), the F-actin stain detected many more stress fibers (Fig. 6B) as compared with 7 days postplating (Fig. 6A).

To understand the structural assembly of F-actin filaments within microspikes, we imaged them at high resolution (Zeiss, 100× water immersion objective, 1.0 NA; Fig. 7). Staining with phalloidin shows F-actin distribution within microspikes, and the punctuate spots (arrows and white circles) of aggregated F-actin (Fig. 7A) and diffuse F-actin (Fig. 7B) possibly at the substrate adhesion sites. These structures must be composed of filamentous actin because specificity of phalloidin binding to F-actin *vs* G-actin is well established.

In addition, by using specific dyes to label mitochondria and actin fibers separately, we obtained fluorescence intensity profiles across the cells as indicated by white vertical and horizontal lines seen in Figs. 4, 6 and 7 in side boxes. These profiles could be used to develop methods to quantify the average number of the actin fibers, where each peak refers to assembled F-actin feature. The thickness of these features could also be measured as the thickness of one peak refers to the size of the F-actin feature. It can be colocalized with the distribution of a mitochondrial stain.

Dynamic imaging of actin detects its reorganization during migration of glioma cells within ECMs

To study real time reorganization of actin within live ACBT glioblastoma cells we transiently transfected the cells with CellularLights Actin-GFP reagent (Fig. 8). Time-lapse data were collected for 2 h with 5 min intervals between recordings. The nonmigrating, rounded live ACBT glioblastoma cells presented very intense GFP fluorescence (white arrow in Fig. 8a–c).

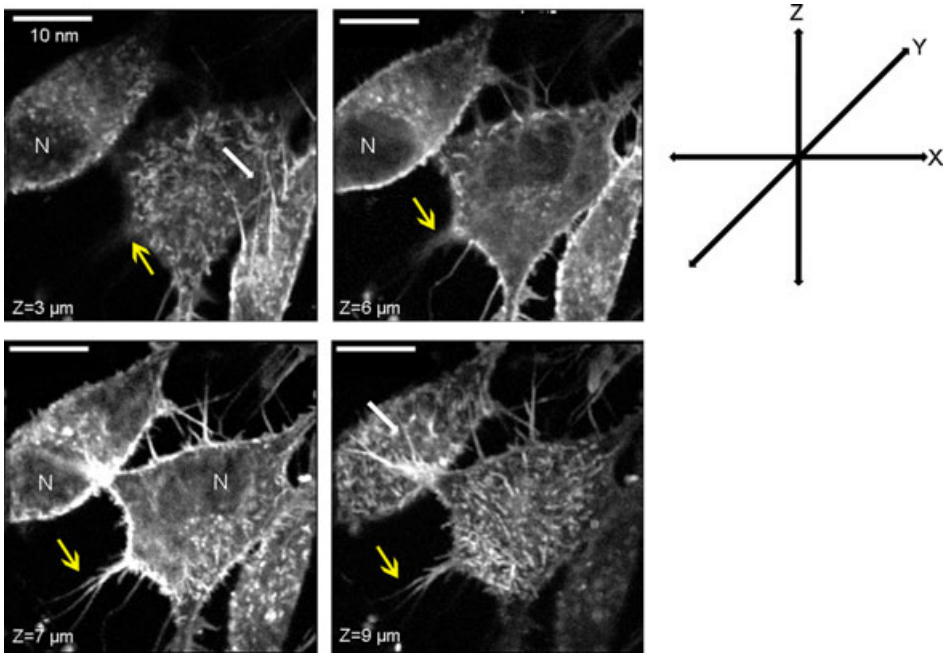

Figure 5. The distribution of F-actin filaments throughout the glioma cells that prior to F-actin stain had functional mitochondria. A variety of F-actin filaments can be seen in the *x–y* optical sections that are cut along the *z*-direction. Scale bar is 8 μm. The $z = 3$ μm and $z = 9$ μm optical sections show F-actin filaments anchoring one cell to another (white arrows). The $z = 7$ μm, $z = 6$ μm as well as $z = 3$ μm and $z = 9$ μm optical sections all display microspikes also called filopodia extending from the cells (larger yellow arrows). Fluorescence emission was isolated through the 500–550 nm filter. Scales are indicated.

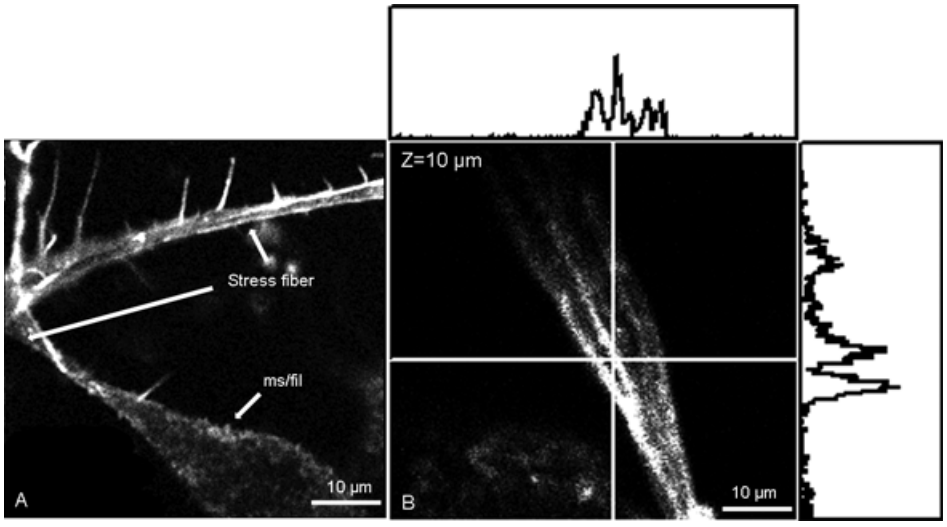

Figure 6. The multiphoton images of F-actin inside the ABCT glioma cells at different postplating stages of cell migration within the three-dimensional collagen hydrogels. (A) Alexa Fluor 488 Phalloidin labeled F-actin assembly in a semimigrating cell, *x–y* plane. A variety of F-actin types of assembly are observed. The migratory section of the cell is characterized by stress fibers and lamellipodia. Nonmigratory section of the cell is composed of microspikes/filopodia (ms/fil). The cells were allowed to migrate for 7 days. (B) Alexa Fluor 488 Phalloidin-labeled F-actin assembly in glioma cells allowed to migrate for 3 days. More stress fibers are observed as compared with 7 days postplating.

We found ACBT glioblastoma cells to dynamically modulate their GFP expression as they migrated within the ECM. The GFP fluorescence appeared to be spreading through the cell body into the lamellipodia (white star next to cell body in Fig. 8a–c) in dynamic bursts, creating temporary pools or ''globes.'' These features possibly represent G-actin generated to facilitate cellular movement along the collagen fibers of the ECM.

DISCUSSION

The leading edge in investigations of human cancers lies in making use of 3D *in vitro* models that can mimic the *in vivo* environment (44). These models resemble more accurately physiological tumor settings, allow expedient experimental manipulations and are more amenable to imaging compared with animals.

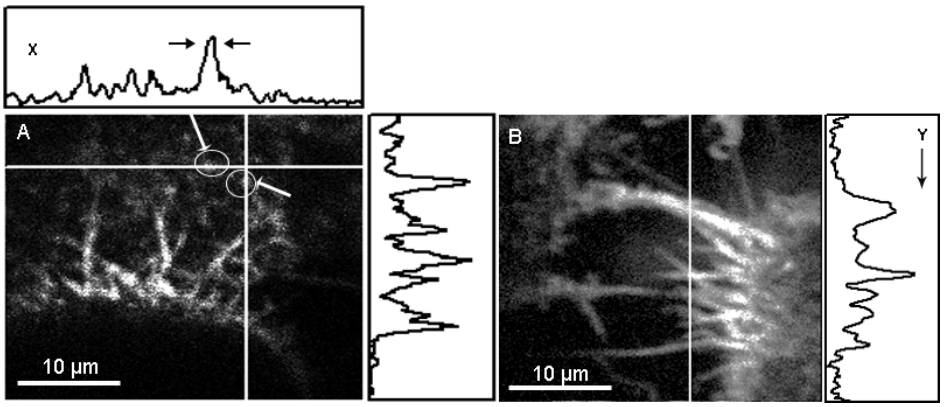

Figure 7. High-resolution images of F-actin distribution inside the microspikes of ABCT glioma cell. Fluorescence of phalloidin AlexaFluor 488 conjugate shows F-actin distribution within microspikes. Focusing objective (Zeiss; 100× water immersion; NA is 1.0) was used to collect images. Fluorescence intensity profiles across the cell as indicated by white lines are displayed in the side boxes. (A) Punctuate spots of aggregated F-actin (circles and white arrows). The F-actin spots are 1.4 μm as estimated from the half-width of the peaks in the fluorescence intensity profiles. (B) Diffuse F-actin at the substrate adhesion sites is observed.

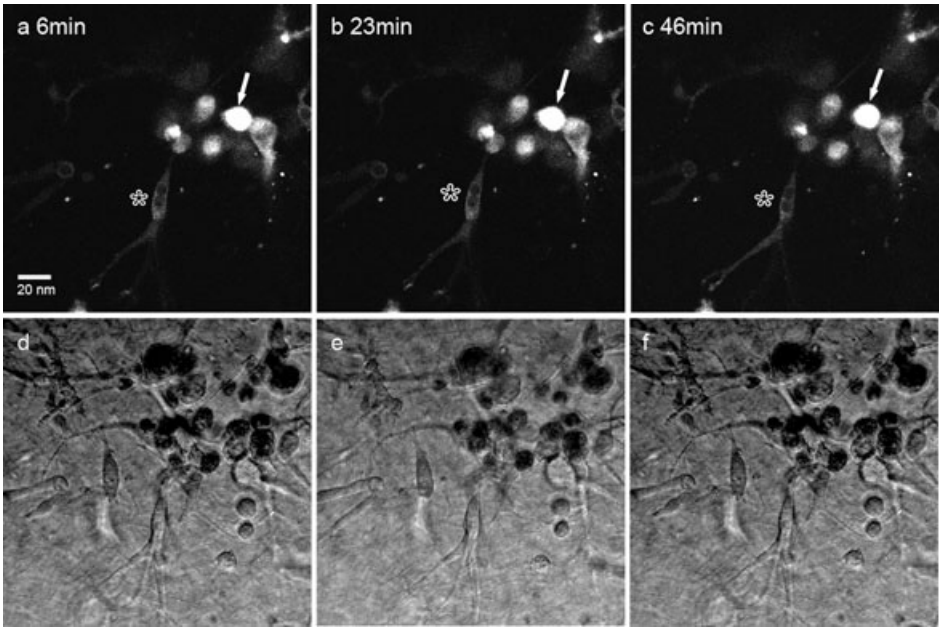

Figure 8. LSM510 time-lapse recordings of live ACBT glioblastoma cells migrating off the spheroid. Spheroid was 100 μm. Focusing objective (40× dry) was used to collect the images (264 μm × 264 μm); (a–c) *en face* confocal fluorescence images show migration of GFP-actin-expressing cells in three-dimensional collagen hydrogels. The cells migrate in all directions; (d–f) true focus *en face* white light images that correspond to the confocal fluorescence images in parts (a–c).

Our work describes an application of multiphoton optical microscopy to study behaviors of glioma tumors in their 3D surroundings aimed to emulate the *in vivo* environments. Specifically, we followed mitochondrial energy metabolism and distribution of actin filaments within the migrating cells of the 3D ACBT glioblastoma model consisting of solid spheroids embedded in the hydrogel ECMs. For the imaging studies presented in this work, collagen is employed as a substrate hydrogel material because it generates a dependable, characterized second harmonic signal that does not bleach. During the development of our optical methods, we routinely use this collagen spectroscopic signature to attain rapid approximate calibrations of the imaging depth. This unique signature is also used to understand the overall 3D structure of the material surrounding embedded spheroids, cells and spheroids that migrate away from them. A development of subcellular imaging based on intrinsic fluorescence of migrating glioma cells embedded in thick "tissue-like" materials, took precedence over focusing on "a biologically correct" ECM material that glioma cells could be exposed to *in vivo*.

Gliomas typically consist of a group of proliferative cells in the tumor mass (often with a necrotic core), surrounded by a shell of invasive, motile cells. The highly invasive cells outside the necrotic core infiltrate diffusely into nearby healthy brain parenchyma and often follow the same anatomical structures along which neural stem cells migrate during development and after brain injury (such as white matter tracts and along the

subependyma). They can also migrate along the brain vasculature by way of the perivascular spaces (28). Because individual cells spread diffusely and at a distance from the core, surgery to remove the bulk of the tumor typically results in the return of the tumor within centimeters of the resection cavity (28). The chemotherapy and radiation therapy have poor efficacy and typically fail, because these treatments are mostly effective against proliferating cells in the tumor core, rather than nonmitotic invading cells. The migrating cells, therefore, became a focus of this imaging study.

To migrate, cells undergo cytoskeletal remodeling to elongate in the direction of migration, and pseudopodia, lamellipodia, filopodia and invadopodia form at the leading invasive edges (30). Actin polymerization at the leading edges appears to be critical for these extensions. Transmembrane integrins expressed in invading cells interact with ECM proteins and with the intracellular actin cytoskeleton (*via* adaptor proteins). The integrins transduce signals between the ECM and actin cytoskeleton to permit transient adhesion to the ECM thus modulating migration. Once transient attachment is established, the extensions can be contracted to advance the cell through the brain tissue (45).

The actin filament distribution within the cytoskeletal network is routinely visualized using immunocytochemistry with fluorescently labeled phalloidin (46). To date, a majority of cellular studies have employed such actin stain in cells confined to a two-dimensional (2D) environment. These earlier works (46) implied that MPM imaging of actin filament distribution using this technology is not as good as confocal visualization. Our imaging work shows that it is not the case. As seen in the present report, in the actin visualization experiments, the high contrast of multiphoton imaging compensates well for its lower resolution. We construct clear images of F-actin filaments extending outward from the cells, anchored appearance of these filaments to the surrounding collagen and clear participation of these filaments in cell–cell interactions.

Much evidence accumulated in support of the claim that the ECM can influence organization of a cell's cytoskeleton (47). Specifically, assembly and disassembly of F-actin filaments was identified as one of the mediators allowing ECM to alter the growth and differentiation of the malignant glioma cells. These observations are not yet well understood, but in several cases results suggest that malignant cells proliferate with no adhesion to the substratum and are characterized by the failure to assemble stress fibers (48). The imaging methods allowed us to discover a previously unknown dynamic pooling of actin in the migrating glioblastoma cells as well as structural difference in the actin fibers formed during the early stages of cell migration (3 days) as compared with 7 days postplating. These discoveries could contribute to the explanation of the migration phenomenon of glioma cells and potentially lead to the development of new cancer therapies.

The earlier reports utilizing 3D collagen matrices (49) to study cellular migration observed cancer cells often to exhibit a collective movement. This collective movement is expected to correlate with cancer invasiveness because such a cluster migration strategy is hypothesized to be more efficient, as it allows both passive and active translocation of heterogeneous sets of cells, therefore promoting spread of cells differing in makeup and functionality (49). Imaging in a 2D plane or confocal microscopy (50) renders a lot of this information unattainable. For example, in a separate experiment (unpublished data), using confocal imaging on the LSM510 system utilizing 488 nm laser excitation wavelength we attempted high-resolution visualization of the actin microspikes extending from the glioma cells into the 3D matrix (alike to those seen in Fig. 5, the 9 μm cut from the cell surface). We could not achieve the same visualization with confocal imaging.

Another essential element of glioblastoma cell migration is energy balance required to support rapid reorganization of actin cytoskeletal elements, mitochondrial ATP production as well as motor protein activity (51). Multiphoton ratiometric redox fluorometry based on cellular fluorescence from reduced NADH and oxidized FAD has been proposed as a tool to study mitochondrial energy changes and metabolism (52). Using this tool, the mitochondrial energy changes in the biological systems have been previously addressed in several earlier studies (53–61). Recent publications range from exploring the potential to image relative amounts of these fluorophores to noninvasively monitoring changes in metabolism in cancerogenesis (62), evaluating necrosis in skin flaps (63) and serving as an indicator for photodynamic therapy (64). In our migrating glioma cells, the mitochondrial redox index value was 0.9 as determined from the most intensely fluorescing x–y optical sections inside the cells. There was no merit in imaging the NADH/FAD fluorescence signals from the lamellopodia of the glioma cells. We believe that the long exposure times during imaging through the entire 3D volume, which took about 15 min, was a main reason for the observation of a subset of cells (40%) that became disrupted. This disruption, therefore, can be avoided by having shorter exposure times. The 60% of the imaged cells were fine and behaved normal as verified by observing them to readily migrate after multiphoton imaging and to subsequently uptake the mitochondrial dye Mitotraker Orange (a sign of normally functioning mitochondria).

We quantified the uptake rate of Mitotraker Orange and show that in the type of 3D hydrogel model we employ, the live migrating glioma cells take up the mitochondrial dye in approximately 2 h. According to a standard protocol supplied by the manufacturer, MitoTracker Orange dye is generally added for 15–45 min to the cells grown on coverslips (2D cell cultures) inside the Petri dish filled with the appropriate culture medium. These exposure times are insufficient to stain mitochondria in the glioma cells migrating in the 3D environments. Alternatively, some researchers use overnight and longer exposures. We observed a clear increase in cell toxicity for the overnight staining treatments. Interestingly, we observed a distinctive difference in mitochondrial morphology detected with native *vs* dye-stained signals (Fig. 2A *vs* Fig. 3C). One possible cause for this effect is that intrinsic mitochondrial signals are much weaker than signals from the mitochondrial dyes, and emit only from certain parts of the mitochondrial assembly. Alternatively, addition of mitochondrial dyes could induce a different mitochondrial appearance.

Inside the cells, the mitochondrial movement, morphology and possibly function is potentially regulated by the cytoskeletal system (65). For example, in *Saccharomyces cerevisiae*, it was demonstrated that mitochondria bind to the actin cytoskeleton that serves as a scaffold for the mitochondrial movement toward their destinations. In upper

eukaryotic cells, the movement of mitochondria, its shape and function is thought to be a result of coordinated interactions of actin filaments (microfilaments), microtubules and intermediate filaments. The imaging methods developed in this work, for the first time provide high resolution and contrast spatial 3D maps for the location of actin filaments with respect to mitochondria within migrating ACBT glioblastoma cells.

CONCLUSIONS

In this report we describe several interesting behaviors of live ACBT glioblastoma cells embedded within the 3D collagen hydrogels. This model aimed to emulate the *in vivo* environments of ACBT proliferation and migration and was characterized by *in situ* MPM. At least three discernible types of cells are present in this model although the live migrating ACBT glioblastoma cells are the focus of this work. We observe that the live migrating ACBT glioblastoma cells' sensitivity to femtosecond laser irradiation employed in MPM imaging is not uniform. *In situ* multiphoton ratiometric redox imaging based on cellular fluorescence from reduced NADH and oxidized FAD detects at least two different populations of migrating ACBT glioblastoma cells. One population of cells maintains original morphology after the 3D imaging, as well as retains functional mitochondria. Another population is characterized by disruption of cellular membranes upon exposure to the focused laser excitation. Although it is not clear if this observation is specific to our *in vitro* model, it implies the potential therapeutic properties of focused nonlinear excitation in the treatment of gliomas.

To complement the existing knowledge that cell–cell body contacts occur through actin fibers, we gain new important details on these interactions in 3D with previously unachievable high resolution and contrast suitable for quantification. Monitoring fluorescence because of GFP expression in live ACBT glioma cells allows us to image the pattern for the dynamic modulation of actin during migration. To our knowledge, we image for the first time the creation of temporary pools or ''globes'' of actin during this important process in 3D and in real time. The imaging methods developed in this work could allow for more sophisticated analysis of whether this property is a general feature of metastatic cells. If this is a case, it might be possible to develop new cancer therapies that specifically target cells with pooled actin.

Additionally, we can detect the spatial distribution of actin in ACBT glioma cells with respect to mitochondria and believe it may be possible to work out an unexplored link between the functional performance of mitochondria, actin distributions and glioma invasiveness in 3D. Understanding these processes can serve as a basis for development of novel cancer diagnostic and treatment tools.

Acknowledgements—This work has been supported in part by George E. Hewitt Medical Fellowship (J.G.L.), NIH Laser Microbeam and Medical Program (LAMMP) at the Beckman Laser Institute, UC Irvine (P41-RR01192), by the Air Force Office of Scientific Research (AFOSR) under agreement number FA95 50-04-1-0101, by UC Riverside Graduate Fellowship (Y.-J.H.), UC Riverside startup research funds (J.G.L.), NSF CAREER Award CBET-0847070 (J.G.L.) and NSF BRIGE Award EEC-0927297 (J.G.L.).

REFERENCES

1. Denk, W., J. H. Strickler and W. W. Webb (1990) Two-photon laser scanning fluorescence microscopy. *Science* **248**, 73–76.
2. Xu, C., W. Zipfel, J. B. Shear, R. M. Williams and W. W. Webb (1996) Multiphoton fluorescence excitation: New spectral window for biological nonlinear microscopy. *Proc. Natl. Acad. Sci. USA* **93**, 10763–10768.
3. Guo, Y., H. E. Savage, F. Liu, S. P. Schantz, P. P. Ho and R. R. Alfano (1999) Subsurface tumor progression investigated by noninvasive optical second harmonic tomography. *Proc. Natl. Acad. Sci. USA* **96**, 10854–10856.
4. Campagnola, P. J., M. D. Wei, A. Lewis and L. M. Loew (1999) High-resolution nonlinear optical imaging of live cells by second harmonic generation. *Biophys. J.* **77**, 3341–3349.
5. So, P. T. C., C. Y. Dong, B. Masters and K. M. Berland (2000) Two-photon excitation fluorescence microscopy. *Annu. Rev. Biomed. Eng.* **2**, 399–429.
6. Moreaux, L., O. Sandre, M. Blanchard-Desce and J. Mertz (2000) Membrane imaging by simultaneous second-harmonic generation and two-photon microscopy. *Opt. Lett.* **25**, 320–322.
7. Gauderon, R., P. B. Lukins and S. J. Sheppard (2001) Optimization of second-harmonic generation microscopy. *Micron* **32**, 691–700.
8. Hopt, A. and E. Neher (2001) Highly nonlinear photodamage in two-photon fluorescence microscopy. *Biophys. J.* **80**, 2029–2036.
9. Yeh, A. T., N. Nassif, A. Zoumi and B. J. Tromberg (2002) Selective corneal imaging using combined second-harmonic generation and two-photon excited fluorescence. *Opt. Lett.* **27**, 2082–2084.
10. Zoumi, A., A. Yeh and B. J. Tromberg (2002) Imaging cells and extracellular matrix in vivo by using second-harmonic generation and two-photon excited fluorescence. *Proc. Natl. Acad. Sci. USA* **99**, 11014–11019.
11. Wong, B. J. F., V. Wallace, M. Coleno, H. P. Benton and B. J. Tromberg (2002) Two-photon excitation laser scanning microscopy of human, porcine, and rabbit nasal septal cartilage. *Tissue Eng.* **7**, 599–606.
12. Ragan, T. R., H. Huang and P. T. C. So (2003) In vivo and ex vivo tissue applications of two-photon microscopy. *Methods Enzymol.* **361**, 481–506.
13. Brown, E., T. McKee, E. DiTomaso, A. Pluen, B. Seed and Y. Boucher (2003) Dynamic imaging of collagen and its modulation in tumors in vivo using second-harmonic generation. *Nat. Med.* **9**, 796–801.
14. Zipfel, W. R., R. M. Williams, R. Christie, A. Y. Nikitin, B. T. Hyman and W. W. Webb (2003) Live tissue intrinsic emission microscopy using multiphoton-excited native fluorescence and second harmonic generation. *Proc. Natl. Acad. Sci. USA* **100**, 7075–7080.
15. Rubart, M. (2004) Two-photon microscopy of cells and tissues. *Circ. Res.* **95**, 1154–1166.
16. Lyubovitsky, J. G., T. B. Krasieva, J. A. Spencer, B. Andersen and B. J. Tromberg (2005) Imaging corneal pathology in a transgenic mouse model using nonlinear microscopy. *J. Biomed. Opt.* **11**, 014013.
17. Helmchen, F. and W. Denk (2005) Deep tissue two-photon microscopy. *Nat. Methods* **2**, 932–940.
18. Diaspro, A., G. Chirico and M. Collini (2005) Two-photon fluorescence excitation and related techniques in biological microscopy. *Q. Rev. Biophys.* **38**, 97–166.
19. Dunn, K. W. and P. A. Young (2006) Principles of multiphoton microscopy. *Nephron Exp. Nephrol.* **3**, e33–e40.
20. Svoboda, K. a. Y. R. (2006) Principles of two-photon excitation microscopy and its applications to neuroscience. *Neuron* **50**, 823–839.
21. Leppert, J., J. Krajewski, S. R. Kantelhardt, S. Schlaffer, N. Petkus, E. Reusche, G. Huttmann and A. Giese (2006) Multiphoton excitation of autofluorescence of glioma tissue. *Neurosurgery* **58**, 759.
22. Benninger, R. K. P., M. Hao and D. W. Piston (2008) Multiphoton excitation imaging of dynamic processes in living cells and tissues. *Rev. Physiol. Biochem. Pharmacol.* **160**, 71–92.

23. Hänninen, P., J. Soukka and J. T. Soini (2008) Two-photon excitation fluorescence bioassays. *Ann. N Y Acad. Sci.* **1130**, 320–326.
24. Hess, K. R., K. R. Broglio and M. L. Bondy (2004) Adult glioma incidence trends in the United States, 1977–2000. *Cancer* **101**, 2293–2299.
25. Larjavaara, S., R. Mäntylä, T. Salminen, H. Haapasalo, J. Raitanen, J. Jääskeläinen and A. Auvinen (2007) Incidence of gliomas by anatomic location. *Neuro Oncol.* **9**, 319–325.
26. Altaner, C. (2008) Glioblastoma and stem cells. *Neoplasma* **55**, 369–374.
27. Sontheimer, H. (2008) A role for glutamate in growth and invasion of primary brain tumors. *J. Neurochem.* **105**, 287–295.
28. Nakada, M., S. Nakada, T. Demuth, N. L. Tran, D. B. Hoelzinger and M. E. Berens (2007) Molecular targets of glioma invasion. *Cell. Mol. Life Sci.* **64**, 458–478.
29. Wallner, K. E., J. H. Galicich, G. Krol, E. Arbit and M. G. Malkin (1989) Patterns of failure following treatments for glioblastoma multiform and anaplastic astrocytoma. *Int. J. Radiat. Oncol. Biol. Phys.* **16**, 1405–1409.
30. Lefranc, F., J. Brotchi and R. Kiss (2005) Possible future issues in the treatment of glioblastomas: Special emphasis on cell migration and the resistance of migrating glioblastoma cells to apoptosis. *J. Clin. Oncol.* **23**, 2411–2422.
31. Boldogh, I. R. and L. A. Pon (2006) Interactions of mitochondria with the actin cytoskeleton. *Biochim. Biophys. Acta* **1763**, 450–462.
32. Madsen, S. J., C. H. Sun, B. J. Tromberg, V. Cristini, N. Magalhaes and H. Hirschberg (2006) Multicell tumor spheroids in photodynamic therapy. *Lasers Surg. Med.* **38**, 555–564.
33. Kleihues, P. and W. K. Cavenee (2000) *World Health Organization Classification of Tumours of the Nervous System*. WHO/IARC, Lyon.
34. Louis, D. N. (2006) Molecular pathology of malignant gliomas. *Annu. Rev. Pathol. Mech. Dis.* **1**, 97–117.
35. Schoenberg, B. S. (1983) The epidemiology of central nervous system tumors. In *Oncology of the Nervous System* (Edited by M. D. Wsaran), p. 1. Martinus Nijhoff, Boston.
36. Hirschberg, H., C. H. Sun, T. B. Krasieva and S. J. Madsen (2006) Effects of ALA-mediated photodynamic therapy on the invasiveness of human glioma cells. *Lasers Surg. Med.* **38**, 939–945.
37. Madsen, S. J., C. H. Sun, B. J. Tromberg, V. Wallace and H. Hirschberg (2000) Photodynamic therapy of human glioma spheroids using 5-aminolevulinic acid. *Photochem. Photobiol.* **72**, 128–134.
38. Sutherland, R. M. and R. E. Durand (1976) Radiation response of muticell spheroids—An in vitro tumor model. *Curr. Top. Radiat. Res.* **11**, 87–139.
39. Molecular Probes. Phallotoxins. Available at: http://probes.invitrogen.com/media/pis/mp00354.pdf. Accessed on 7 January 2011.
40. Dunn, A. K., V. P. Wallace, M. Coleno, M. W. Berns and B. J. Tromberg (2000) Influence of optical properties on two-photon fluorescence imaging in turbid samples. *Appl. Opt.* **39**, 1194–1201.
41. LaMorte, V. J., A. Zoumi and B. J. Tromberg (2003) Spectroscopic approach for monitoring two-photon excited FRET from homodimers at the subcelluar level. *J. Biomed. Opt.* **8**, 357–361.
42. Lyubovitsky, J. G., T. B. Krasieva, J. A. Spencer, B. Andersen and B. J. Tromberg (2005) Corneal damage revealed by endogenous cellular fluorescence and second harmonic signals from collagen. *Proc. SPIE* **5700**, 213–217.
43. Parka, C. Y., Z. Zhua, C. Zhanga, C. S. Moona and R. S. Chuck (2006) Cellular redox state predicts *in vitro* corneal endothelial cell proliferation capacity. *Exp. Eye Res.* **83**, 903–910.
44. Yamada, K. M. and E. Cukierman (2007) Modeling tissue morphogenesis and cancer in 3D. *Cell* **130**, 601–610.
45. Bellail, A. C., S. B. Hunter, D. J. Brat, C. Tan and E. G. Van Meir (2004) Microregional extracellular matrix heterogeneity in brain modulates glioma cell invasion. *Int. J. Biochem. Cell Biol.* **36**, 1046–1069.
46. Small, J. V., K. Rottner, P. Hahne and K. I. Andersen (1999) Visualizing the actin cytoskeleton. *Microsc. Res. Tech.* **47**, 3–17.
47. Nagano, N., M. Aoyagi, K. Hirakawa, M. Yamamoto and K. Yamamoto (1996) Organization of F-actin filaments in human glioma cell lines cultured on extracellular matrix proteins. *J. Neurooncol.* **27**, 215–224.
48. Volk, T., B. Geiger and A. Raz (1984) Motility and adhesive properties of high- and low-metastatic murine neoplastic cells. *Cancer Res.* **44**, 811–824.
49. Hegerfeldt, Y., M. Tusch, E. B. Brocker and P. Friedl (2002) Collective cell movement in primary melanoma explants: Plasticity of cell–cell interactions, beta1-integrin function, and migration strategies. *Cancer Res.* **62**, 2125–2130.
50. Caspani, E. M., D. Echevarria, K. Rottner and J. V. Small (2006) Live imaging of glioblastoma cells in brain tissue shows requirement of actin bundles for migration. *Neuron Cell Biol.* **2**, 105–114.
51. de Cavanagh, E. M., M. Ferder, F. Inserra and L. Ferder (2009) Angiotensin II, mitochondria, cytoskeletal, and extracellular matrix connections: An integrating viewpoint. *Am. J. Physiol. Heart Circ. Physiol.* **296**, H550–H558.
52. Huang, S., A. A. Heikal and W. W. Webb (2002) Two-photon fluorescence spectroscopy and microscopy of NAD(P)H and flavoprotein. *Biophys. J.* **82**, 2811–2825.
53. Chance, B., P. Cohen, F. Jobsis and B. Schoener (1962) Intracellular oxidation-reduction states in vivo. *Science* **137**, 499–508.
54. Chance, B. and M. Lieberman (1978) Intrinsic fluorescence emission from the cornea at low temperatures: Evidence of mitochondrial signals and their differing redox states in epithelial and endothelial sides. *Exp. Eye Res.* **26**, 111–117.
55. Chance, B., I. A. Salkovitz and A. G. B. Kovach (1972) Kinetics of mitochondrial flavoprotein and pyridine nucleotide in perfused heart. *Am. J. Physiol.* **223**, 207–218.
56. Croce, A. C., A. Ferrigno, M. Vairetti, R. Bertone, I. Freitas and G. Bottiroli (2004) Autofluorescence properties of isolated rat hepatocytes under different metabolic conditions. *Photochem. Photobiol. Sci.* **3**, 920–926.
57. Kunz, W. and W. Kunz (1985) Contribution of different enzymes to flavoprotein fluorescence in isolated rat liver mitochondria. *Biochim. Biophys. Acta* **841**, 237–246.
58. Kuznetsov, A. V., O. Mayboroda, D. Kunz, K. Winkler, W. Schubert and W. S. Kunz (1998) Functional imaging of mitochondria in saponin-permeabilized mice muscle fibers. *J. Cell Biol.* **140**, 1091–1099.
59. Kuznetsov, A. V., Y. Usson, X. Leverve and R. Margreiter (2004) Subcellular heterogeneity of mitochondrial function and dysfunction: Evidence obtained by confocal imaging. *Mol. Cell. Biochem.* **256**, 359–365.
60. Masters, B. R., P. T. C. So and E. Gratton (1998) Optical biopsy of in vivo human skin: Multi-photon excitation microscopy. *Lasers Med. Sci.* **13**, 196–203.
61. Romashko, D. N., E. Marban and B. O'Rourke (1998) Subcellular metabolic transients and mitochondrial redox waves in heart cells. *Proc. Natl. Acad. Sci. USA* **95**, 1618–1623.
62. Skala, M. C., K. M. Riching, A. Gendron-Fitzpatrick, J. Eickhoff, K. W. Eliceiri, J. G. White and N. Ramanujam (2007) In vivo multi-photon microscopy of NADH and FAD redox states, fluorescence lifetimes and cellular morphology in precancerous epithelia. *Proc. Natl. Acad. Sci. USA* **104**, 19494–19499.
63. Mokry, M., P. Gal, M. Harakalova, Z. Hutnanova, J. Kusnir, S. Mozes and J. Sabo (2007) Experimental study on predicting skin flap necrosis by fluorescence in the FAD and NADH bands during surgery. *Photochem. Photobiol.* **83**, 1193–1196.
64. Zhang, Z., D. Blessington, H. Li, T. M. Busch, J. Glickson, Q. Luo, B. Chance and G. Zheng (2004) Redox ratio of mitochondria as an indicator for the response of photodynamic therapy. *J. Biomed. Opt.* **9**, 772–778.
65. Anesti, V. and L. Scorrano (2006) The relationship between mitochondrial shape and function and cytoskeleton. *Biochim. Biophys. Acta* **1757**, 692–699.